Observability Analysis for the INS Error Model with GPS/Uncalibrated Magnetometer Aiding

Ronan Arraes Jardim Chagas[1] and Jacques Waldmann[2]

***Abstract*— A stand-alone inertial navigation system (INS) yields time-diverging solutions due to errors in the inertial sensors, which can inhibit long term navigation. To circumvent this issue, a set of non-inertial sensors is used to limit these errors. The fusion between additional data and INS solution is often done by means of an extended Kalman filter using a state-error model. However, the Kalman filter estimates can only be used if the system is fully observable. This paper has analyzed conditions to achieve full observability using as non-inertial sensors a GPS receiver and an uncalibrated magnetometer with an IMU mounted on a locally horizontal-stabilized platform and with a strapdown IMU. The magnetometer data errors was considered to be constant and the resulting vector was added to the state space. The observability for all scenarios has been verified when the system dynamics is piece-wise constant, and the analysis has been carried out using concepts of linear algebra to provide results that are geometrically meaningful. The novel results obtained have been verified by covariance analysis using a simulated INS. Also, it was shown by simulations that the uncalibrated data fusion from the magnetometer without proper processing would yield in estimation divergence.**

I. Introduction

A stand-alone inertial navigation system (INS) yields time-diverging solutions due to errors in the inertial measurement unit (IMU) sensors [1], that is accelerometers and rate-gyros arranged in their respective orthogonal triads. In myriad applications, such errors can preclude the use of the navigation solution in the long term. To circumvent this issue, a set of non-inertial sensors often aid the INS by means of a state-error model embedded in an extended Kalman filter [1]. The state-error model employs a state vector that comprises position and velocity errors, misalignment angles with respect to the locally horizontal coordinate frame, accelerometer biases, and rate-gyro drifts [1]. Consequently, observability analysis is called for to ensure that the filter estimates are accurate. Only with full observability the estimation error covariance can decrease to a minimum in all state-error space directions, and just then Kalman filter estimates can be used to correct the INS errors and calibrate the inertial sensors [2].

Navigation becomes unfeasible when based on a low-quality IMU and aiding sensors are lacking to limit the misalignment error. These errors can be bounded by a magnetometer or a camera. The latter requires a pointing apparatus and calls for image processing. Hence, for low cost systems, the magnetometer is the usual choice of aiding sensor, along with a pressure altimeter, and embedded in many comercially available IMUs [3], [4].

A previous study of the authors investigated the observability of the INS error model with GPS/calibrated magnetometer aiding [5]. It turned out that such device can provide measurements related to the position and misalignment errors when the magnetometer raw data is compared to a embedded geomagnetic field model. However, if this model is not accurate enough or if magnetometer calibration has not been executed correctly, then the usual measurement model presented in [5] for the magnetometer will possess errors. In such case, these errors must be estimated or it could severely degraded the estimation accuracy as shown here by simulations.

For the sake of modeling simplicity, it has been assumed that the effect of the aforementioned errors in the magnetometer measurement model can be modeled as a constant, called as the magnetometer bias. The observability analysis of the INS error model when the magnetometer bias is added to the space state is then carried out for an IMU mounted on a stabilized platform and for a strapdown IMU. In both cases, piece-wise constant dynamics for the INS error model have been assumed as in [6], [7]. The theoretical results was confirmed by covariance analysis using a simulated INS with ideal sensors. Also, to cover more realistic situations, two simulations were executed considering a non-ideal INS and a time-varying magnetometer bias. In the first, the magnetometer bias was neglected and, in the second, it was estimated by the Kalman filter.

Sections II and III present coordinate frames and a glossary of acronyms, respectively. The INS error model and the sensors model are presented in sections IV and V, respectively. The observability analysis is shown in section VI. Simulations and results are presented in section VII. Finally, the conclusions are written in section VIII.

II. Coordinate frames

The **true local horizontal frame** is used to represent the INS errors. In the true vehicle position, its X-axis points towards north, its Y-axis points towards east, and its Z-axis points down. This coordinate system is thereafter indicated with the l subscript.

The **computed coordinate frame** is defined as the local horizontal frame at the position computed by the INS. It is

*This work was financially supported by the project FINEP/CTA/INPE SIA (Inertial Systems for Aerospace Application, in Portuguese)

[1]Ronan Arraes Jardim Chagas is a Ph.D. student at Instituto Tecnológico de Aeronáutica (Technological Institute of Aeronautics), Division of Electronics Engineering, 12.228-900 SP São José dos Campos, Brazil ronan.jardim at gmail.com

[2]Jacques Waldmann is an Associate Professor at Instituto Tecnológico de Aeronáutica (Technological Institute of Aeronautics), Division of Electronics Engineering, 12.228-900 SP São José dos Campos, Brazil jacques at ita.br

thereafter indicated with the c subscript.

The **platform coordinate frame** is defined as the local horizontal frame computed by the INS. It is thereafter indicated with the p subscript.

The **body coordinate frame** is defined as the inertial sensors coordinate frame. It is usually assumed to be aligned with the vehicle coordinate frame in strapdown IMUs or aligned with the platform coordinate frame in IMUs mounted on a stabilized platform. This coordinate frame is thereafter indicated with the b subscript.

III. Notation and Abbreviations

$\mathbb{R}$	Set of real numbers
DCM	Direction Cossine Matrix
y	Scalar
$\mathbf{y}$	Vector
$\mathbf{A}$	Matrix
$diag(\mathbf{A}\ \mathbf{B})$	Block-diagonal matrix constructed by the matrices $\mathbf{A}$ and $\mathbf{B}$.
$\mathbf{I}_n$	Identity matrix of size n.
$[\mathbf{y}]_\times \mathbf{x}$	Matrix representation of the cross product $\mathbf{y} \times \mathbf{x}$.
$\mathbf{D}_a^b$	DCM that rotates from the a coordinate frame to the b coordinate frame.
$\boldsymbol{\omega}_c^{ab}$	Angular rate of the a coordinate frame with respect to the b coordinate frame represented in the c coordinate frame.
$\boldsymbol{\rho}_l$	Transport rate represented in the local horizontal frame.
$\boldsymbol{\Omega}_{e,l}$	Earth's angular rate represented in the local horizontal frame.
$\mathbf{Asp}_l$	Specific force represented in the local horizontal frame.
$\boldsymbol{\Delta}\mathbf{R}_l$	INS position error represented in the local horizontal frame.
$\boldsymbol{\Delta}\mathbf{V}_l$	INS velocity error represented in the local horizontal frame.
$\boldsymbol{\Psi}$	Misalignment from the computed coordinate frame to the platform coordinate frame.
$\boldsymbol{\nabla}$	Bias of the accelerometers.
$\boldsymbol{\epsilon}$	Drift of the rate-gyros.
R_N	North-south radius of curvature of the Earth.
R_E	East-west radius of curvature of the Earth.
R_e	Earth radius at the latitude of the vehicle.
g_e	Gravitation at the latitude of the vehicle.
λ	Latitude of the vehicle.
h	Altitude of the vehicle.
$\boldsymbol{\omega}_l^{li}$	Angular rate of the local horizontal frame with respect to the inertial coordinate frame represented in the local horizontal frame, which is equal to $\boldsymbol{\Omega}_{e,l} + \boldsymbol{\rho}_l$.

IV. INS error model

INS errors are increasing and unbounded, thus navigation can be seriously compromised in a long-term mission even with high-quality inertial sensors [1], [8], [5]. To circumvent this problem, a set of non-inertial sensors provides additional information that can limit such errors. The fusion between the non-inertial sensors and the INS solution is often accomplished by an extended Kalman filter using a state-error model. The usual state vector for the INS error model is composed of position and velocity errors, misalignment from the computed coordinate frame to the platform coordinate frame, accelerometers triad bias, and rate-gyros triad drift [1], [8]. Here, the magnetometer bias is also added as an additional state as described in section V.

For the sake of completeness, the standard state-error model for an IMU mounted on a stabilized platform and for a strapdown IMU are presented in eqs. 1 and 2, respectively:

$$\dot{\mathbf{x}} = \left[\begin{array}{c|c|c|c|c} [\boldsymbol{\rho}_l]_\times & \mathbf{I}_{3\times3} & \mathbf{0}_{3\times3} & \mathbf{0}_{3\times3} & \mathbf{0}_{3\times3} \\ \mathbf{g}_e & \boldsymbol{\alpha} & \boldsymbol{\Gamma} & \mathbf{I}_{3\times3} & \mathbf{0}_{3\times3} \\ \mathbf{0}_{3\times3} & \mathbf{0}_{3\times3} & \boldsymbol{\beta} & \mathbf{0}_{3\times3} & -\mathbf{I}_{3\times3} \\ \mathbf{0}_{3\times3} & \mathbf{0}_{3\times3} & \mathbf{0}_{3\times3} & \mathbf{0}_{3\times3} & \mathbf{0}_{3\times3} \\ \mathbf{0}_{3\times3} & \mathbf{0}_{3\times3} & \mathbf{0}_{3\times3} & \mathbf{0}_{3\times3} & \mathbf{0}_{3\times3} \end{array}\right] \mathbf{x} \quad (1)$$

$$\mathbf{x} = \left[\begin{array}{ccccc} \boldsymbol{\Delta}\mathbf{R}_l^T & \boldsymbol{\Delta}\mathbf{V}_l^T & \boldsymbol{\psi}^T & \boldsymbol{\nabla}_l^T & \boldsymbol{\epsilon}_l^T \end{array}\right]^T$$

$$\dot{\mathbf{x}} = \left[\begin{array}{c|c|c|c|c} [\boldsymbol{\rho}_l]_\times & \mathbf{I}_{3\times3} & \mathbf{0}_{3\times3} & \mathbf{0}_{3\times3} & \mathbf{0}_{3\times3} \\ \mathbf{g}_e & \boldsymbol{\alpha} & \boldsymbol{\Gamma} & \mathbf{D}_l^b & \mathbf{0}_{3\times3} \\ \mathbf{0}_{3\times3} & \mathbf{0}_{3\times3} & \boldsymbol{\beta} & \mathbf{0}_{3\times3} & -\mathbf{D}_l^b \\ \mathbf{0}_{3\times3} & \mathbf{0}_{3\times3} & \mathbf{0}_{3\times3} & \mathbf{0}_{3\times3} & \mathbf{0}_{3\times3} \\ \mathbf{0}_{3\times3} & \mathbf{0}_{3\times3} & \mathbf{0}_{3\times3} & \mathbf{0}_{3\times3} & \mathbf{0}_{3\times3} \end{array}\right] \mathbf{x} \quad (2)$$

$$\mathbf{x} = \left[\begin{array}{ccccc} \boldsymbol{\Delta}\mathbf{R}_l^T & \boldsymbol{\Delta}\mathbf{V}_l^T & \boldsymbol{\psi}^T & \boldsymbol{\nabla}_b^T & \boldsymbol{\epsilon}_b^T \end{array}\right]^T$$

where $\mathbf{g}_e = diag\left(\begin{array}{ccc} -g_e/R_e & -g_e/R_e & 2g_e/R_e \end{array}\right)$, $\boldsymbol{\alpha} = [\boldsymbol{\rho}_l + 2\boldsymbol{\Omega}_{e,l}]_\times$, $\boldsymbol{\beta} = [\boldsymbol{\rho}_l + \boldsymbol{\Omega}_{e,l}]_\times$, and $\boldsymbol{\Gamma} = [\mathbf{Asp}_{l,j}]_\times$.

If the observables directly measure the position and velocity errors, then, by definition, those state vector components are observable. The position error is dynamically coupled only with the velocity error, which shows that the position error dynamics fails to bring any unmeasured component into the observable subspace. Hence, for the sake of simplicity of the observability analysis, the position error component can be neglected [9].

V. Sensors model

This investigation concentrates on INS error-state observability analysis when a GPS receiver and an uncalibrated magnetometer aid the INS, which extends a previous study of the authors [5]. A measurement model for each non-inertial sensor is described next.

The GPS observables are assumed to directly provide position and velocity errors. In practice, GPS raw data can be post-processed to yield vehicle position and velocity in the WGS84 ellipsoid coordinate frame as in a loosely-coupled implementation. Alternatively, the raw data composed of, for example, pseudo-ranges and Doppler shift between the receiver and the satellites are employed in a tightly-coupled implementation [8]. The GPS observables are then compared to the INS solution to produce a measurement vector of the state-error. Receiver clock errors have not been involved in this investigation.

The GPS measurement equation under the aforementioned assumption and neglecting measurement noise is presented in eq. 3:

$$\mathbf{y}_{GPS} = \begin{bmatrix} \mathbf{I}_3 & \mathbf{0}_3 & \mathbf{0}_3 & \mathbf{0}_3 & \mathbf{0}_3 \\ \mathbf{0}_3 & \mathbf{I}_3 & \mathbf{0}_3 & \mathbf{0}_3 & \mathbf{0}_3 \end{bmatrix} \mathbf{x} \tag{3}$$

The calibrated magnetometer model can be seen in [5], although it is also presented next for the sake of completeness.

The magnetometer observables are composed of the difference between the magnetometer raw data and the INS-based local geomagnetic field vector. Considering Pinson's model [10], the DCM from the body coordinate frame to the true local horizontal frame can be approximated by neglecting second order terms as in eq. 4:

$$\begin{aligned} \mathbf{D}_b^l &= \mathbf{D}_b^p \cdot \mathbf{D}_p^c \cdot \mathbf{D}_c^l \approx \\ &\approx \mathbf{D}_b^p \cdot (\mathbf{I}_{3\times3} - [\boldsymbol{\psi}]_\times) \cdot (\mathbf{I}_{3\times3} - [\Delta\boldsymbol{\theta}]_\times) \approx \\ &\approx \mathbf{D}_b^p \cdot (\mathbf{I}_{3\times3} - [\boldsymbol{\psi}]_\times - [\Delta\boldsymbol{\theta}]_\times) \end{aligned} \tag{4}$$

where $\Delta\boldsymbol{\theta}_k$ is the misalignment from the true coordinate frame to the computed coordinate frame and $\boldsymbol{\psi}$ is misalignment from the computed coordinate frame to the platform coordinate frame. Thus, the calibrated magnetometer measurement neglecting noise can be approximated by:

$$\begin{aligned} &\mathbf{B}_{mag} \approx \mathbf{D}_b^p \cdot (\mathbf{I}_{3\times3} - [\boldsymbol{\psi}]_\times - [\Delta\boldsymbol{\theta}]_\times) \cdot \mathbf{B}_l \\ &\mathbf{D}_b^p \mathbf{B}_{mag} - \mathbf{B}_l \approx -[\boldsymbol{\psi}]_\times \mathbf{B}_l - [\Delta\boldsymbol{\theta}]_\times \mathbf{B}_l \\ &\mathbf{y}_{mag}^{cal} = [\mathbf{B}_l]_\times \boldsymbol{\psi} + [\mathbf{B}_l]_\times \Delta\boldsymbol{\theta} \end{aligned} \tag{5}$$

where $\mathbf{B}_{mag}$ is the raw magnetometer measurement and $\mathbf{B}_l$ is the local geomagnetic field vector represented in the true local horizontal frame, which is not accessible. The latter is usually obtained from a geomagnetic field model using the position solution either computed by the GPS or by the INS. It is straightforward to check that $\mathbf{D}_b^p = \mathbf{I}_3$ if the IMU and the magnetometer are mounted on a stabilized platform. Moreover, vector $\Delta\boldsymbol{\theta}$ can be related to the position error represented in the local horizontal frame as in eq. 6:

$$\begin{aligned} \Delta\boldsymbol{\theta} &= \begin{bmatrix} 0 & \frac{1}{R_E+h} & 0 \\ -\frac{1}{R_N+h} & 0 & 0 \\ 0 & -\frac{\tan\lambda}{R_E+h} & 0 \end{bmatrix} \cdot \Delta\mathbf{R}_l = \\ &= \mathbf{C} \cdot \Delta\mathbf{R}_l \end{aligned} \tag{6}$$

Finally, the calibrated magnetometer measurement can be approximated by:

$$\mathbf{y}_{mag}^{cal} = \begin{bmatrix} \mathbf{C} \cdot [\mathbf{B}_l]_\times & \mathbf{0}_3 & [\mathbf{B}_l]_\times & \mathbf{0}_3 & \mathbf{0}_3 \end{bmatrix} \mathbf{x} = \mathbf{H}_{mag}^{cal} \mathbf{x} \tag{7}$$

If the geomagnetic field model $\mathbf{B}_l$ is not accurate enough or if the magnetometer calibration has not been executed correctly, then the model $\mathbf{y}_{mag}^{cal}$ in eq. 7 will possess errors. Thus, the uncalibrated magnetometer raw measurement can be approximated as follows:

$$\mathbf{B}_{mag} \approx \mathbf{D}_b^p \cdot (\mathbf{I}_{3\times3} - [\boldsymbol{\psi}]_\times - [\Delta\boldsymbol{\theta}]_\times) \cdot \mathbf{B}_l + \boldsymbol{\delta}_b \tag{8}$$

where the component $\boldsymbol{\delta}_b$ comprises the aforementioned errors.

As mentioned before, it has been considered that the error $\boldsymbol{\delta}_b$ can be modeled as a constant, which was called the magnetometer bias, because it is expected that this vector varies slowly when represented in the body coordinate frame for the situations of interest. However, later in the simulations, this restriction is relaxed and the measurement error $\boldsymbol{\delta}_b$ is simulated using a time-varying function. Hence, for the sake of modeling simplicity, the magnetometer bias dynamics neglecting the model noise can be written as in eq. 9:

$$\dot{\boldsymbol{\delta}}_b = \mathbf{0}_{3\times1} \tag{9}$$

Additionally, the magnetometer bias can be added to the space-state yielding to an extended INS error model presented in eqs. 10 and 11 for an IMU mounted on a stabilized platform and for a strapdown IMU, respectively:

$$\begin{aligned} \dot{\mathbf{x}}_e &= \left[\begin{array}{c|c|c|c|c|c} [\boldsymbol{\rho}_l]_\times & \mathbf{I}_{3\times3} & \mathbf{0}_{3\times3} & \mathbf{0}_{3\times3} & \mathbf{0}_{3\times3} & \mathbf{0}_{3\times3} \\ \mathbf{g}_e & \boldsymbol{\alpha} & \boldsymbol{\Gamma} & \mathbf{I}_{3\times3} & \mathbf{0}_{3\times3} & \mathbf{0}_{3\times3} \\ \mathbf{0}_{3\times3} & \mathbf{0}_{3\times3} & \boldsymbol{\beta} & \mathbf{0}_{3\times3} & -\mathbf{I}_{3\times3} & \mathbf{0}_{3\times3} \\ \mathbf{0}_{3\times3} & \mathbf{0}_{3\times3} & \mathbf{0}_{3\times3} & \mathbf{0}_{3\times3} & \mathbf{0}_{3\times3} & \mathbf{0}_{3\times3} \\ \mathbf{0}_{3\times3} & \mathbf{0}_{3\times3} & \mathbf{0}_{3\times3} & \mathbf{0}_{3\times3} & \mathbf{0}_{3\times3} & \mathbf{0}_{3\times3} \\ \mathbf{0}_{3\times3} & \mathbf{0}_{3\times3} & \mathbf{0}_{3\times3} & \mathbf{0}_{3\times3} & \mathbf{0}_{3\times3} & \mathbf{0}_{3\times3} \end{array}\right] \mathbf{x}_e \\ \mathbf{x}_e &= \begin{bmatrix} \Delta\mathbf{R}_l^T & \Delta\mathbf{V}_l^T & \boldsymbol{\psi}^T & \boldsymbol{\nabla}_l^T & \boldsymbol{\epsilon}_l^T & \boldsymbol{\delta}_p^T \end{bmatrix}^T \end{aligned} \tag{10}$$

$$\begin{aligned} \dot{\mathbf{x}}_e &= \left[\begin{array}{c|c|c|c|c|c} [\boldsymbol{\rho}_l]_\times & \mathbf{I}_{3\times3} & \mathbf{0}_{3\times3} & \mathbf{0}_{3\times3} & \mathbf{0}_{3\times3} & \mathbf{0}_{3\times3} \\ \mathbf{g}_e & \boldsymbol{\alpha} & \boldsymbol{\Gamma} & \mathbf{D}_l^b & \mathbf{0}_{3\times3} & \mathbf{0}_{3\times3} \\ \mathbf{0}_{3\times3} & \mathbf{0}_{3\times3} & \boldsymbol{\beta} & \mathbf{0}_{3\times3} & -\mathbf{D}_l^b & \mathbf{0}_{3\times3} \\ \mathbf{0}_{3\times3} & \mathbf{0}_{3\times3} & \mathbf{0}_{3\times3} & \mathbf{0}_{3\times3} & \mathbf{0}_{3\times3} & \mathbf{0}_{3\times3} \\ \mathbf{0}_{3\times3} & \mathbf{0}_{3\times3} & \mathbf{0}_{3\times3} & \mathbf{0}_{3\times3} & \mathbf{0}_{3\times3} & \mathbf{0}_{3\times3} \\ \mathbf{0}_{3\times3} & \mathbf{0}_{3\times3} & \mathbf{0}_{3\times3} & \mathbf{0}_{3\times3} & \mathbf{0}_{3\times3} & \mathbf{0}_{3\times3} \end{array}\right] \mathbf{x}_e \\ \mathbf{x}_e &= \begin{bmatrix} \Delta\mathbf{R}_l^T & \Delta\mathbf{V}_l^T & \boldsymbol{\psi}^T & \boldsymbol{\nabla}_b^T & \boldsymbol{\epsilon}_b^T & \boldsymbol{\delta}_b^T \end{bmatrix}^T \end{aligned} \tag{11}$$

The models in eqs. 10 and 11 without the position errors, which were neglected, are thereafter called models 1 and 2, respectively.

Thus, the uncalibrated magnetometer measurement equation can be written as follows:

$$\begin{aligned} \mathbf{y}_{mag}^{uncal} &= \mathbf{H}_{mag}^{cal} \mathbf{x} + \mathbf{D}_p^b \boldsymbol{\delta}_b \\ \mathbf{y}_{mag}^{uncal} &= \left[\begin{array}{c|c} \mathbf{H}_{mag}^{cal} & \mathbf{D}_p^b \end{array}\right] \mathbf{x}_e \end{aligned} \tag{12}$$

VI. Observability Analysis

From the INS error dynamics in eqs. 10 and 11, one concludes that it is a time-varying, linear system. The most general way to check observability is to compute the observability Grammian [11]. However, it leads to such complicated mathematical treatment that it is unfeasible for the addressed problem.

In the literature, observability has been verified by three main methods. The first is to analyze conditions that turn the model into a time-invariant system, e. g. the vehicle is stationary on the Earth's surface, or to find an adequate Lyapunov transformation that also leads to a time-invariant system. Thus the observability can be checked by means

of rank computation of the observability matrix [11]. This approach was used in [1], [12].

The second method is applicable to piece-wise constant (PWC) systems. The observability analysis is still done by rank computation, but it turns out that it can be greatly simplified when a certain condition holds as is presented in Theorem 1 [9]. For the INS error model 1, the system can be considered PWC if the specific force is piece-wise constant [6]. For the INS error model 2, the system can be approximated by a PWC system if the specific force and attitude with respect to the local horizontal frame are piece-wise constant [7]. In this case, it is also expected that the DCM $\mathbf{D}_p^b$ will be PWC, since, during a maneuver segment, it will vary only due to numerical errors and imperfections of the inertial sensors. Thus, for sufficiently short segments, the uncalibrated magnetometer measurement matrix in eq. 12 can be approximated as a PWC matrix.

The third method has tried to investigate observability without assuming piece-wise constant dynamics [12], [13], [14], [15], [16]. Since the observability analysis of time-varying systems is not easily applied under general conditions, several restrictions can be considered, for example, constant specific forces and angular velocities, or a C-shaped path.

For the sake of simplicity, the second method based on assuming piece-wise constant dynamics has been preferred here. It can be shown that under this constraint, an observability analysis with linear algebra concepts provides sufficient conditions for full observability that hold for practically all situations of interest [5]. Additionally, the approach yields a geometrical insight of the kinematics involved in the observability analysis [5]. Let a vehicle move at constant altitude according to three consecutive trajectory segments: 1) towards North; 2) in a C-shaped trajectory; and 3) towards East. The composed movement leads to a time-varying INS error model. However, if segment 2 is neglected, then the above INS error models turn into PWC systems. Thus, if full observability by the end of segment 3 can be proved, then, by definition, the time-varying system composed of the three segments is also fully observable. However, if full observability cannot be claimed from the analysis of the first and the third PWC segments, then further analysis including the second segment is needed. For practically all the situations of interest, the vehicle can move in such a manner that the INS error model will remain constant during certain time intervals. Thus the analysis of just these segments using the aforementioned method can provide sufficient conditions for full observability [5].

A. Observability Analysis of Piece-Wise Constant Systems

A PWC system is defined as in eq. 13:

$$\begin{aligned} \dot{\mathbf{x}} &= \mathbf{A}_j\mathbf{x} + \mathbf{B}_j\mathbf{u} \\ \mathbf{y} &= \mathbf{C}_j\mathbf{x} \end{aligned} \tag{13}$$

where $j \in [0, 1, 2, \cdots]$ and matrices $\mathbf{A}_j$, $\mathbf{B}_j$, and $\mathbf{C}_j$ are constants for all j. Observability can be checked by rank analysis of the total observability matrix (TOM), defined as in eq. 14 for the first $r+1$ segments [9]:

$$\bar{\mathbf{Q}}(r) = \begin{bmatrix} \bar{\mathbf{Q}}_0 \\ \bar{\mathbf{Q}}_1 \cdot e^{A_0\Delta_0} \\ \vdots \\ \bar{\mathbf{Q}}_r \cdot e^{\mathbf{A}_{r-1}\Delta_{r-1}} \cdot \ \ \cdots \ \ \cdot e^{\mathbf{A}_1\Delta_1} \cdot e^{\mathbf{A}_0\Delta_0} \end{bmatrix} \tag{14}$$

with matrix $\mathbf{Q}_i$ defined as in eq. 15:

$$\bar{\mathbf{Q}}_i = \begin{bmatrix} \mathbf{C}_i^T & [\mathbf{C}_i\mathbf{A}_i]^T & \cdots & \left[\mathbf{C}_i\mathbf{A}_i^{n-1}\right]^T \end{bmatrix}^T \tag{15}$$

where n is the state vector dimension.

The computation of the exponential matrices leads to tedious and complicated algebraic calculations, but it can be avoided if the following theorem holds [9].

Theorem 1: If:

$$NULL(\mathbf{Q}_j) \in NULL(\mathbf{A}_j), \quad \forall\ j\ \in [0, 1, 2, \cdots, r]$$

then the following holds:

$$\begin{aligned} NULL(\bar{\mathbf{Q}}(r)) &= NULL(\bar{\mathbf{Q}}_s(r)) \\ RANK(\bar{\mathbf{Q}}(r)) &= RANK(\bar{\mathbf{Q}}_s(r)) \end{aligned}$$

where $\bar{\mathbf{Q}}_s(r)$ is the stripped observability matrix (SOM) defined in eq. 16.

$$\bar{\mathbf{Q}}_s(r) = \begin{bmatrix} \bar{\mathbf{Q}}_0^T & \bar{\mathbf{Q}}_1^T & \cdots & \bar{\mathbf{Q}}_r^T \end{bmatrix}^T \tag{16}$$

Thus the computation of the exponential matrices can be avoided in the observability analysis.

Proof: See [9]. ■

[9], [7] stated that the Theorem 1 holds for both models in eqs. 1 and 2 when GPS measurements are available. On the other hand, [5] showed that this theorem only holds for these models if the specific force $\mathbf{Asp}_l$ is not aligned with the angular rate of the local horizontal frame with respect to the inertial coordinate frame $\boldsymbol{\omega}_l^{li}$ at any segment. However, to the best knowledge of the authors, the Theorem 1 validity has not been checked yet for the models 1 and 2, in which the magnetometer bias is added to the state vector.

For the model 2, the observability matrix for the *j*-th segment can be written, after elementary row operations, as in eq. 17:

$$\bar{\mathbf{Q}}_j = \left[\begin{array}{cccccc|c} \mathbf{I}_3 & \mathbf{0}_3 & \mathbf{0}_3 & \mathbf{0}_3 & \mathbf{0}_3 & \mathbf{0}_3 & \\ \mathbf{0}_3 & \boldsymbol{\Gamma}_j & \mathbf{D}_{l,j}^b & \mathbf{0}_3 & \mathbf{0}_3 & \mathbf{0}_3 & \\ \mathbf{0}_3 & \boldsymbol{\Gamma}_j\boldsymbol{\beta} & \mathbf{0}_3 & -\boldsymbol{\Gamma}_j\mathbf{D}_{l,j}^b & \mathbf{0}_3 & \mathbf{0}_3 & \text{GPS} \\ \mathbf{0}_3 & \boldsymbol{\Gamma}_j\boldsymbol{\beta}^2 & \mathbf{0}_3 & -\boldsymbol{\Gamma}_j\boldsymbol{\beta}\mathbf{D}_{l,j}^b & \mathbf{0}_3 & \mathbf{0}_3 & \\ \vdots & \vdots & \vdots & \vdots & \vdots & \vdots & \\ \hline \mathbf{0}_3 & [\mathbf{B}_l]_\times & \mathbf{0}_3 & \mathbf{0}_3 & \mathbf{0}_3 & \mathbf{D}_{p,j}^b & \\ \mathbf{0}_3 & [\mathbf{B}_l]_\times\boldsymbol{\beta} & \mathbf{0}_3 & [\mathbf{B}_l]_\times\mathbf{D}_{l,j}^b & \mathbf{0}_3 & \mathbf{0}_3 & \text{Mag.} \\ \mathbf{0}_3 & [\mathbf{B}_l]_\times\boldsymbol{\beta}^2 & \mathbf{0}_3 & [\mathbf{B}_l]_\times\boldsymbol{\beta}\mathbf{D}_{l,j}^b & \mathbf{0}_3 & \mathbf{0}_3 & \\ \vdots & \vdots & \vdots & \vdots & \vdots & \vdots & \end{array}\right] \tag{17}$$

where the subscript *j* indicates a matrix at *j*-th segment. Notice that matrix $\boldsymbol{\beta}$, which is the cross product matrix of

the angular rate vector $\boldsymbol{\omega}_l^{li}$, and the matrix $[\mathbf{B}_l]_\times$ are time-varying. However, they can be approximated as constants for a short term analysis if the terrestrial speed is small enough.

A vector $\mathbf{x} \in NULL(\bar{\mathbf{Q}}_j)$ must satisfy the following conditions:

$$\begin{cases} (1) & \mathbf{x}_1 = \mathbf{0}_{3\times1} \\ (2) & \boldsymbol{\Gamma}_j\mathbf{x}_2 + \mathbf{D}_{l,j}^b\mathbf{x}_3 = \mathbf{0}_{3\times1} \\ (3) & \boldsymbol{\Gamma}_j\boldsymbol{\beta}^n(\boldsymbol{\beta}\mathbf{x}_2 - \mathbf{D}_{l,j}^b\mathbf{x}_4) = \mathbf{0}_{3\times1} \quad n \in [0,1,2,\cdots] \\ (4) & [\mathbf{B}_l]_\times\boldsymbol{\beta}^n(\boldsymbol{\beta}\mathbf{x}_2 - \mathbf{D}_{l,j}^b\mathbf{x}_4) = \mathbf{0}_{3\times1} \quad n \in [1,2,\cdots] \\ (5) & [\mathbf{B}_l]_\times\mathbf{x}_2 + \mathbf{D}_{l,j}^b\mathbf{x}_5 = \mathbf{0}_{3\times1} \end{cases} \tag{18}$$

If $\mathbf{Asp}_{l,j}$ is not aligned with $\boldsymbol{\omega}_l^{li}$, then condition (3) and Theorem A.4 lead to $\boldsymbol{\beta}\mathbf{x}_2 - \mathbf{D}_{l,j}^b\mathbf{x}_4 = \mathbf{0}_{3\times1}$.

Furthermore, the following conditions must be satisfied if the vector $\mathbf{x}$ also lies in the null space of the *j*-th segment dynamics matrix $\mathbf{A}_j$:

$$\begin{aligned} \boldsymbol{\alpha}_j\mathbf{x}_1 + \boldsymbol{\Gamma}_j\mathbf{x}_2 + \mathbf{D}_{l,j}^b\mathbf{x}_3 &= \mathbf{0}_{3\times1} \\ \boldsymbol{\beta}_j\mathbf{x}_2 - \mathbf{D}_{l,j}^b\mathbf{x}_4 &= \mathbf{0}_{3\times1} \end{aligned} \tag{19}$$

It is straight forward to check that if $\mathbf{x} \in NULL(\bar{\mathbf{Q}}_j)$ and $\mathbf{Asp}_{l,j}$ is not aligned with $\boldsymbol{\omega}_l^{li}$, then $\mathbf{x}$ also lies in the $\mathbf{A}_j$ null space. Hence, if this is valid for all $j \geq 0$, then Theorem 1 holds. One should notice that this proof can be extended to the model 1 by substituting $\mathbf{D}_l^b = \mathbf{I}_3$ and $\mathbf{D}_b^p = \mathbf{I}_3$.

Hereafter, the assumption that $\mathbf{Asp}_{l,j}$ is not aligned with $\boldsymbol{\omega}_l^{li}$ for all $j \geq 0$ is called assumption $\star$. Thus, if assumption $\star$ holds, the observability analysis for the models 1 and 2 with GPS and uncalibrated magnetometer measurements can be carried out by means of rank analysis of the SOM.

B. Observability Analysis for an IMU Mounted on a Stabilized Platform

The observability analysis for the model 1, when GPS and uncalibrated magnetometer measurements as in eqs. 3 and 12, respectively, are available, is hereafter presented. The SOM for the first three segments can be assembled after elementary row and column operations as in eq. 20.

$$\bar{\mathbf{Q}}_r^{'}(2) = \left[\begin{array}{ccccc} \mathbf{I}_{3\times3} & \mathbf{0}_{3\times3} & \mathbf{0}_{3\times3} & \mathbf{0}_{3\times3} & \mathbf{0}_{3\times3} \\ \mathbf{0}_{3\times3} & \mathbf{0}_{3\times3} & \mathbf{I}_{3\times3} & \mathbf{0}_{3\times3} & \mathbf{0}_{3\times3} \\ \mathbf{0}_{3\times3} & \mathbf{0}_{3\times3} & \mathbf{0}_{3\times3} & -\boldsymbol{\Gamma}_0 & \mathbf{0}_{3\times3} \\ \vdots & \vdots & \vdots & \vdots & \vdots \\ \mathbf{0}_{3\times3} & \mathbf{0}_{3\times3} & \mathbf{0}_{3\times3} & -\boldsymbol{\Gamma}_0\boldsymbol{\beta}^{n-1} & \mathbf{0}_{3\times3} \\ \vdots & \vdots & \vdots & \vdots & \vdots \\ \mathbf{0}_{3\times3} & \mathbf{0}_{3\times3} & \mathbf{0}_{3\times3} & \mathbf{0}_{3\times3} & \mathbf{I}_{3\times3} \\ \mathbf{0}_{3\times3} & \mathbf{0}_{3\times3} & \mathbf{0}_{3\times3} & -[\mathbf{B}_l]_\times & \mathbf{0}_{3\times3} \\ \vdots & \vdots & \vdots & \vdots & \vdots \\ \mathbf{0}_{3\times3} & \mathbf{0}_{3\times3} & \mathbf{0}_{3\times3} & -[\mathbf{B}_l]_\times\boldsymbol{\beta}^{n-1} & \mathbf{0}_{3\times3} \\ \vdots & \vdots & \vdots & \vdots & \vdots \\ \hline \multicolumn{5}{c}{\mathcal{A}_1} \\ \hline \multicolumn{5}{c}{\mathcal{A}_2} \end{array}\right] \tag{20}$$

where:

$$\mathcal{A}_i = \left[\begin{array}{ccccc} \mathbf{0}_{3\times3} & \boldsymbol{\Gamma}_i - \boldsymbol{\Gamma}_0 & \mathbf{0}_{3\times3} & \mathbf{0}_{3\times3} & \mathbf{0}_{3\times3} \\ \mathbf{0}_{3\times3} & \mathbf{0}_{3\times3} & \mathbf{0}_{3\times3} & -\boldsymbol{\Gamma}_i & \mathbf{0}_{3\times3} \\ \vdots & \vdots & \vdots & \vdots & \vdots \\ \mathbf{0}_{3\times3} & \mathbf{0}_{3\times3} & \mathbf{0}_{3\times3} & -\boldsymbol{\Gamma}_i\boldsymbol{\beta}^{n-1} & \mathbf{0}_{3\times3} \\ \vdots & \vdots & \vdots & \vdots & \vdots \end{array}\right] \tag{21}$$

Thus, if $\mathbf{x} \in NULL(\bar{\mathbf{Q}}_r^{'}(2))$, then the following must hold:

$$\begin{aligned} &(1) \quad \mathbf{x}_1 = \mathbf{0}_{3\times1} \\ &(2) \quad \mathbf{x}_3 = \mathbf{0}_{3\times1} \\ &(3) \quad \boldsymbol{\Gamma}_i\boldsymbol{\beta}^n\mathbf{x}_4 = \mathbf{0}_{3\times1}, \quad n \in [0,1,2,\cdots],\ i \in [0,1,2] \\ &(4) \quad [\mathbf{B}_l]_\times\boldsymbol{\beta}^n\mathbf{x}_4 = \mathbf{0}_{3\times1}, \quad n \in [0,1,2,\cdots] \\ &(5) \quad (\boldsymbol{\Gamma}_1 - \boldsymbol{\Gamma}_0)\mathbf{x}_2 = \mathbf{0}_{3\times1} \\ &(6) \quad (\boldsymbol{\Gamma}_2 - \boldsymbol{\Gamma}_0)\mathbf{x}_2 = \mathbf{0}_{3\times1} \end{aligned} \tag{22}$$

Since this analysis is only valid if the assumption $\star$ holds, thus condition (3) and Theorem A.4 lead to $\mathbf{x}_4 = \mathbf{0}_{3\times1}$. Additionally, condition (5) restricts $\mathbf{x}_2$ to be aligned with $\mathbf{Asp}_{l,1} - \mathbf{Asp}_{l,0}$. Likewise, condition (6) also restricts $\mathbf{x}_2$ and $\mathbf{Asp}_{l,2} - \mathbf{Asp}_{l,0}$ to be linearly dependent vectors. Thus, if $\mathbf{Asp}_{l,1} - \mathbf{Asp}_{l,0}$ is not aligned with $\mathbf{Asp}_{l,2} - \mathbf{Asp}_{l,0}$, then the conditions (5) and (6) can only be valid with $\mathbf{x}_2 = \mathbf{0}_{3\times1}$, which leads to a fully observable system.

Finally, the full observability of the piece-wise constant INS error model for an IMU mounted on a stabilized platform with GPS/uncalibrated magnetometer aiding is achieved when:

- The specific force $\mathbf{Asp}_{l,j}$ is not aligned with the angular rate of the local horizontal frame with respect to the inertial coordinate frame $\boldsymbol{\omega}_l^{li}$ at any segment j, $j \in [0,1,2,3,\cdots]$;
- There are at least three segments in which the specific force difference from segment 0 to segment 1 $\mathbf{Asp}_{l,1} - \mathbf{Asp}_{l,0}$ is not aligned with the specific force difference from segment 0 to segment 2 $\mathbf{Asp}_{l,2} - \mathbf{Asp}_{l,0}$.

One should notice that these are the same conditions to achieve full observability in case that the GPS is the only aiding sensor [9]. If the magnetometer is calibrated and the bias can be neglected, then the full observability can be achieved with just two specific force segments [5]. Hence, an uncalibrated magnetometer does not help to improve observability, but the magnetometer bias can be made observable by means of specific force changes if the IMU is mounted on a stabilized platform.

C. Observability Analysis for a strapdown IMU

The observability analysis for the model 2, when GPS and uncalibrated magnetometer measurements as in eqs. 3 and 12, respectively, are available, is hereafter presented. If the strapdown IMU angular rate with respect to the local coordinate frame, when represented in this same frame, is zero, then the observability analysis can be carried out as in

the previous section [5]. Moreover, the INS error model of a strapdown IMU can be also stimulated by rotational motion. Thus additional excitation signals are available to increase the dimension of the observable subspace. The analysis of the scenario in which the IMU undergoes PWC attitude is presented next.

The SOM for the first two segments can be assembled after elementary row and column operations as in eq. 23:

$$\bar{\mathbf{Q}}_r^{'}(1) = \left[\begin{array}{cccc|c} & & & & \mathbf{0}_{9\times3} \\ & \mathcal{A}_0 & & & \vdots \\ & & & & \mathbf{0}_{3\times3} \\ & & & & \vdots \\ \hline & & & & \mathbf{0}_{9\times3} \\ & \mathcal{A}_1 & & & \vdots \\ & & & & \mathbf{0}_{3\times3} \\ & & & & \vdots \\ \hline \mathbf{0}_{3\times3} & [\mathbf{B}_l]_\times & \mathbf{0}_{3\times3} & \mathbf{0}_{3\times3} & \mathbf{D}_{p,0}^b \\ \mathbf{0}_{3\times3} & [\mathbf{B}_l]_\times & \mathbf{0}_{3\times3} & \mathbf{0}_{3\times3} & \mathbf{D}_{p,1}^b \\ \vdots & \vdots & \vdots & \vdots & \vdots \end{array}\right] \tag{23}$$

where:

$$\mathcal{A}_0 = \begin{bmatrix} \mathbf{I}_{3\times3} & \mathbf{0}_{3\times3} & \mathbf{0}_{3\times3} & \mathbf{0}_{3\times3} \\ \mathbf{0}_{3\times3} & \boldsymbol{\Gamma} & \mathbf{D}_{l,0}^b & \mathbf{0}_{3\times3} \\ \mathbf{0}_{3\times3} & \boldsymbol{\Gamma\beta} & \mathbf{0}_{3\times3} & -\boldsymbol{\Gamma}\mathbf{D}_{l,0}^b \\ \vdots & \vdots & \vdots & \vdots \\ \mathbf{0}_{3\times3} & \boldsymbol{\Gamma\beta}^n & \mathbf{0}_{3\times3} & -\boldsymbol{\Gamma\beta}^{n-1}\mathbf{D}_{l,0}^b \\ \vdots & \vdots & \vdots & \vdots \end{bmatrix} \tag{24}$$

$$\mathcal{A}_1 = \begin{bmatrix} \mathbf{0}_{3\times3} & \mathbf{0}_{3\times3} & \mathbf{D}_{l,1}^b - \mathbf{D}_{l,0}^b & \mathbf{0}_{3\times3} \\ \mathbf{0}_{3\times3} & \mathbf{0}_{3\times3} & \mathbf{0}_{3\times3} & -\boldsymbol{\Gamma}(\mathbf{D}_{l,1}^b - \mathbf{D}_{l,0}^b) \\ \vdots & \vdots & \vdots & \\ \mathbf{0}_{3\times3} & \mathbf{0}_{3\times3} & \mathbf{0}_{3\times3} & -\boldsymbol{\Gamma\beta}^{n-1}(\mathbf{D}_{l,1}^b - \mathbf{D}_{l,0}^b) \\ \vdots & \vdots & \vdots & \end{bmatrix} \tag{25}$$

Thus if $\mathbf{x} \in NULL(\bar{\mathbf{Q}}_r^{'}(1))$, then the following must hold:

$$\begin{aligned} &(1) \quad \mathbf{x}_1 = \mathbf{0}_{3\times1} \\ &(2) \quad \boldsymbol{\Gamma}\mathbf{x}_2 + \mathbf{D}_{l,0}^b\mathbf{x}_3 = \mathbf{0}_{3\times1} \\ &(3) \quad \boldsymbol{\Gamma\beta}^n(\boldsymbol{\beta}\mathbf{x}_2 - \mathbf{D}_{l,0}^b\mathbf{x}_4) = \mathbf{0}_{3\times1}, \quad n \in [0,1,2,\cdots] \\ &(4) \quad (\mathbf{D}_{l,1}^b - \mathbf{D}_{l,0}^b)\mathbf{x}_3 = \mathbf{0}_{3\times1} \\ &(5) \quad \boldsymbol{\Gamma\beta}^n(\mathbf{D}_{l,1}^b - \mathbf{D}_{l,0}^b)\mathbf{x}_4 = \mathbf{0}_{3\times1}, \quad n \in [0,1,2,\cdots] \\ &(6) \quad [\mathbf{B}_l]_\times\mathbf{x}_2 + \mathbf{D}_{l,0}^b\mathbf{x}_5 = \mathbf{0}_{3\times1} \\ &(7) \quad [\mathbf{B}_l]_\times\mathbf{x}_2 + \mathbf{D}_{l,1}^b\mathbf{x}_5 = \mathbf{0}_{3\times1} \end{aligned} \tag{26}$$

Conditions (3) and (5), assumption $\star$, and Theorem A.4 lead to (A) $\boldsymbol{\beta}\mathbf{x}_2 - \mathbf{D}_{l,0}^b\mathbf{x}_4 = \mathbf{0}_{3\times1}$ and (B) $(\mathbf{D}_{l,1}^b - \mathbf{D}_{l,0}^b)\mathbf{x}_4 = \mathbf{0}_{3\times1}$. Condition (B) together with Theorem A.5 claim that $\mathbf{x}_4$ must lie in the Euler axis in which a single rotation aligns the body coordinate frame in segment 0 (*b0*) with the body coordinate frame in segment 1 (*b1*) [5]. This axis is thereafter called $\mathbf{e}_{b0\rightleftarrows b1}$. Likewise, $\mathbf{x}_3$ must also lie in the same axis due to condition (4) [5]. Then condition (2) leads to $\boldsymbol{\Gamma}\mathbf{x}_2 = -\mathbf{D}_{l,0}^b\mathbf{x}_3$, which constrains $\mathbf{x}_2$ and the specific force $\mathbf{Asp}_l$ to lie in a plane perpendicular to the Euler axis $\mathbf{e}_{b0\rightleftarrows b1}$ if $\mathbf{x}_3$ is not $\mathbf{0}_{3\times1}$ [5]. In the same way, if $\mathbf{x}_4$ is not $\mathbf{0}_{3\times1}$, then condition (A) above constrains $\mathbf{x}_2$ and the angular rate of the local horizontal frame with respect to the inertial coordinate frame $\boldsymbol{\omega}_l^{li}$ to also lie in a plane perpendicular to the same Euler axis $\mathbf{e}_{b0\rightleftarrows b1}$ [5]. Hence, if either the specific force $\mathbf{Asp}_l$ **or** the angular rate of the local horizontal frame with respect to the inertial coordinate frame $\boldsymbol{\omega}_l^{li}$ is not perpendicular to the Euler axis $\mathbf{e}_{b0\rightleftarrows b1}$, then the components $\mathbf{x}_2$, $\mathbf{x}_3$, and $\mathbf{x}_4$ must all be $\mathbf{0}_{3\times1}$ [5]. If it holds, then it is straightforward to check that $\mathbf{x}_5$ must also be $\mathbf{0}_{3\times1}$, since both $\mathbf{D}_{l,0}^b$ and $\mathbf{D}_{l,1}^b$ are full rank matrices. In such case, the INS error model with GPS and uncalibrated magnetometer aiding is fully observable.

Finally, the full observability of the INS error model for a strapdown IMU with constant specific forces undergoing PWC attitude with GPS/uncalibrated magnetometer aiding is achieved when:

- The specific force $\mathbf{Asp}_l$ is not aligned with the angular rate of the local horizontal frame with respect to the inertial coordinate frame $\boldsymbol{\omega}_l^{li}$;
- The specific force $\mathbf{Asp}_l$ **or** the angular rate of the local horizontal frame with respect to the inertial coordinate frame $\boldsymbol{\omega}_l^{li}$ is not perpendicular to the Euler axis in which a single rotation aligns the body coordinate frame in segment 0 (*b0*) with the body coordinate frame in segment 1 (*b1*) $\mathbf{e}_{b0\rightleftarrows b1}$.

VII. Simulation and Results

The five scenarios proposed to verify the foregoing theoretical results are presented as follows. All numerical simulations were obtained by a simulated INS coded in Matlab.

The three first scenarios verified the INS error model observability by covariance analysis. In these cases, the accelerometers and rate-gyros have been considered ideal and thus the model noise covariance has been set to zero. The initial Kalman filter covariance and GPS and magnetometer measurement noise covariance matrices are presented, respectively, in eqs. 27, 28, and 29 with SI units [5]:

$$\begin{aligned} \mathbf{P}_0 = diag\big(&10^{-6} \;\; 10^{-6} \;\; 10^{-6} \;\; 10^{-4} \;\; 10^{-4} \;\; 10^{-4} \\ &10^{-6} \;\; 10^{-6} \;\; 10^{-6} \;\; 10^{-10} \;\; 10^{-10} \;\; 10^{-10} \\ &10^{-3} \;\; 10^{-3} \;\; 10^{-3}\big) \end{aligned} \tag{27}$$

$$\mathbf{R}_{GPS} = diag\big(10^{-10} \;\; 10^{-10} \;\; 10^{-10}\big) \tag{28}$$

$$\mathbf{R}_{MAG} = diag\big(10^{-20} \;\; 10^{-20} \;\; 10^{-20}\big) \tag{29}$$

For the sake of simplicity, the local geomagnetic field vector has been assumed to point towards north with 230.60 mGauss of intensity, which is the geomagnetic field intensity at the city of São José dos Campos, Brazil. Additionally, the magnetometer bias has been assumed constant as in eq. 30:

$$\boldsymbol{\delta}_b = [10 \;\; 10 \;\; 10]^T \quad \text{mGauss} \tag{30}$$

TABLE I: UAV trajectory for scenario 01

		Specific forces		
Start (s)	**End** (s)	**N** (m/s^2)	**E** (m/s^2)	**D** (m/s^2)
0	20	0	0	-g
20	40	0	0.5	-g
40	60	0.5	0	-g+0.5
60	80	0	0.5	-g+0.5

The first scenario simulates an IMU mounted on a locally horizontal-stabilized platform in a GPS/Magnetometer-aided INS when the vehicle is subjected to the trajectory in Table I. The standard deviations of the state estimation error are presented component-wise in fig. 1.

The second and third scenarios simulates a position-stationary strapdown IMU aided by GPS and magnetometer. The IMU has been subjected to piece-wise attitude changes in which the Euler angles that rotate the local coordinate frame into alignment with the body coordinate frame (yaw, pitch, and roll rotation sequence) are described in the figs. 2a and 2b for the second and third scenarios, respectively. In both cases, the angles have 0.5 s of rise time to avoid the discontinuities of an instantaneously change. Additionally, the standard deviations of the state estimation error are presented component-wise in fig. 3 for the second scenario and in fig. 4 for the third scenario.

The forth and fifth scenarios consider a more realistic situation. In this case, the position error is added to the Kalman filter and the various simulation parameters are presented in Table II. The UAV velocities and angular rates are described in the Appendix B. The magnetometer bias for these both scenarios was simulated according to fig. 2c. In the forth scenario, the eq. 7 was used as the magnetometer measurement equation, thus the magnetometer data were fused neglecting the bias. On the other hand, in the fifth scenario, the measurement equation used for the magnetometer data was eq. 12 and thus the magnetometer bias was estimated by the Kalman filter. The estimation errors of the position and velocity components for the forth scenario are presented in fig. 5, and the estimation errors for each state component for the fifth scenario are presented in figs. 6 and 7.

A. Results Analysis

Figs. 1 to 4 confirm the theoretical results of the observability analysis.

In scenario 01, when an IMU mounted on a stabilized platform is aided by GPS and uncalibrated magnetometer, the INS error model achieves full observability only in the third segment ($t > 40s$).

In scenarios 02 (fig. 3) and 03 (fig. 4), in which a strapdown IMU aided by GPS and uncalibrated magnetometer was simulated, it can be seen that the full observability is achieved for scenario 02 at the third segment ($t > 40s$) and for scenario 03 at the second segment ($t > 20s$). This behavior is explained because, in scenario 02, the Euler axis that rotates the body coordinate frame at the first segment to the body coordinate frame at the second segment points towards east. Since the IMU is stationary, both the specific force and the angular rate of the local coordinate frame with respect to the inertial coordinate frame lie in the XZ plane of the local coordinate frame. Thus, these two vectors are perpendicular to the Euler axis described before. Hence, as the theoretical analysis predicted, this rotation does not bring all state components to the observable subspace. On the other hand, the first rotation in scenario 03 has the Euler axis aligned with the vertical axis of the local horizontal frame. Thus, the Euler axis is not simultaneously perpendicular to the specific force and to the angular rate of the local coordinate frame with respect to the inertial coordinate frame, which brings all state components to the observable subspace.

The comparison between the forth and fifth scenarios show that if the magnetometer bias is high, then the magnetometer data fusion without proper processing would yield in estimation divergence. On the other hand, as one can see in the scenario 05 results, even with the assumption that the magnetometer bias is constant, the technique described here successfully estimated a slowly varying magnetometer bias and avoided the estimation divergence seen in scenario 04.

VIII. Conclusions

The observability of a linear INS error model has been analyzed with aiding sensors that involve the use of GPS and uncalibrated magnetometer when the vehicle trajectory yields piece-wise constant error dynamics. The analysis dealt with both a gyro-stabilized platform undergoing piece-wise constant specific force segments and a strapdown IMU that is also subjected to piece-wise rotation segments.

The magnetometer errors were modeled as a constant vector that was added to the INS error model state space. Thus, the theoretical analysis provided conditions to achieve full observability based on IMU maneuvers. All the results were confirmed by simulations.

Finally, the simulations verified that the estimation accuracy can be severally degraded if the magnetometer bias is neglected. Also, it was verified that the Kalman filter can still properly estimate the state vector even if the magnetometer bias is time-varying with slow dynamics.

Appendix A
Theorems

The theorems on this appendix were already stated in [5], but they are also presented here for the sake of completeness.

Theorem A.1: Let $\mathbf{x} \in \mathbb{R}^3 \neq \mathbf{0}_{3\times1}$ and $\mathbf{y} \in \mathbb{R}^3 \neq \mathbf{0}_{3\times1}$. If $[\mathbf{x}]_\times \mathbf{y} = \mathbf{0}_{3\times1}$, then $\mathbf{x}$ and $\mathbf{y}$ must be aligned.

Proof: The proof is trivial considering that $[\mathbf{x}]_\times \mathbf{y} = \mathbf{x} \times \mathbf{y}$. ■

Theorem A.2: Let $\mathbf{x} \in \mathbb{R}^3 \neq \mathbf{0}_{3\times1}$ and $\mathbf{y} \in \mathbb{R}^3 \neq \mathbf{0}_{3\times1}$. Thus $NULL([\mathbf{y}]_\times [\mathbf{x}]_\times{}^n) = NULL([\mathbf{x}]_\times), n \in [1, 2, 3, 4, \cdots]$, iff $\mathbf{x}$ and $\mathbf{y}$ are not orthogonal.

Proof: Left to the reader due to lack of space. ■

Theorem A.3: Let $\mathbf{x} \in \mathbb{R}^3 \neq \mathbf{0}_{3\times1}$ and $\mathbf{y} \in \mathbb{R}^3 \neq \mathbf{0}_{3\times1}$ be two orthogonal vectors, then the set of vectors $[\mathbf{x}, \mathbf{x} \times \mathbf{y}]$ spans $NULL([\mathbf{y}]_\times [\mathbf{x}]_\times)$.

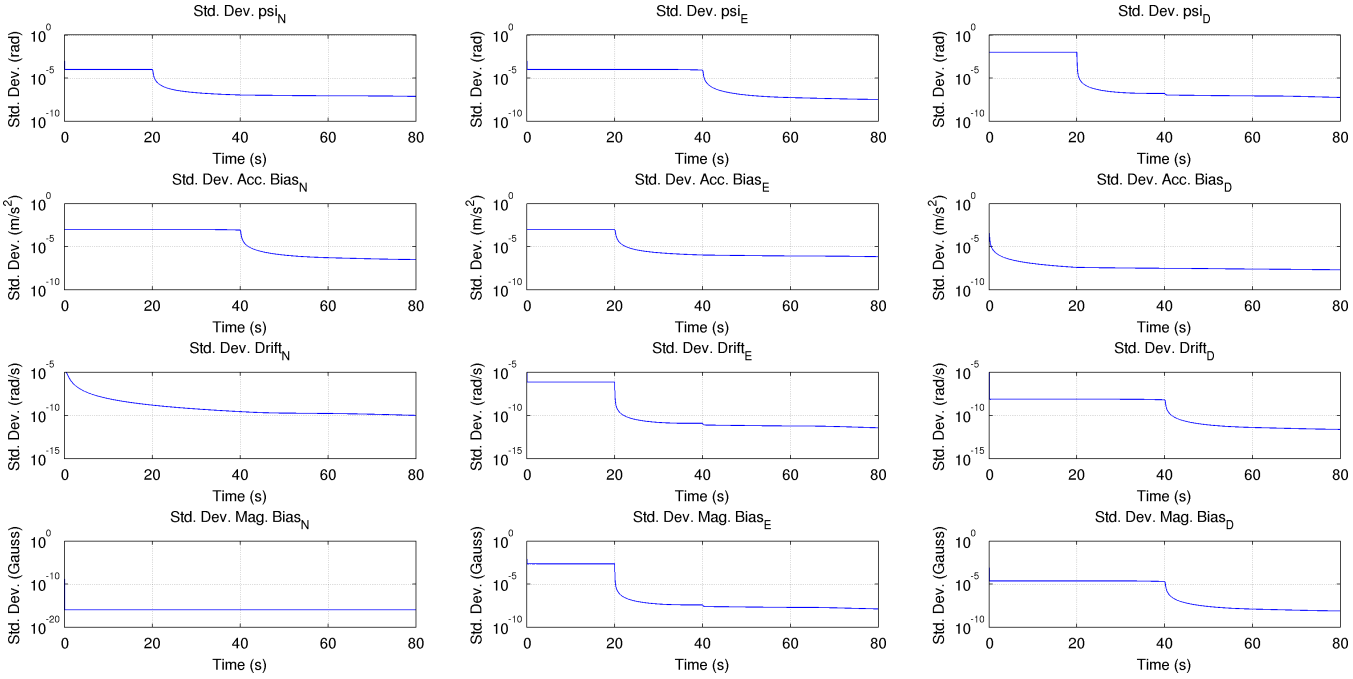

Fig. 1: Scenario 01 - Standard deviations for observability analysis with an IMU mounted on a stabilized platform.

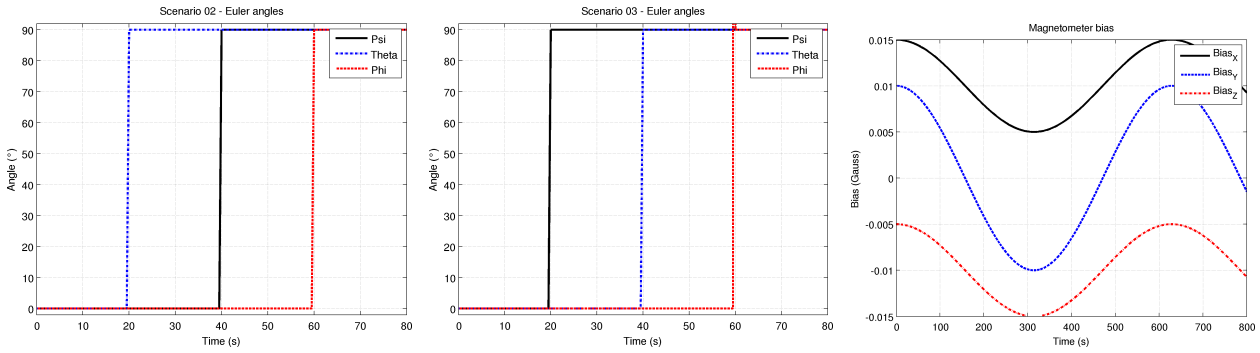

(a) Scenario 02 - Euler angles. (b) Scenario 03 - Euler angles. (c) Scenario 04 and 05 - Magnetometer bias.

Fig. 2: Euler angles for scenarios 02 and 03 and magnetometer bias for scenario 04.

Proof: Left to the reader due to lack of space. ■

Theorem A.4: Let $\mathbf{x} \in \mathbb{R}^3 \neq \mathbf{0}_{3\times1}$ and $\mathbf{y} \in \mathbb{R}^3 \neq \mathbf{0}_{3\times1}$ be two non-collinear vectors. If $[\mathbf{y}]_\times [\mathbf{x}]_\times{}^n \mathbf{v} = \mathbf{0}_{3\times1}$ holds for all $n \in [0, 1, 2, \cdots, L],\ L \geq 1$, then $\mathbf{v} = \mathbf{0}_{3\times1}$ is the only possible solution.

Proof: The proof is trivial considering Theorems A.1, A.2, and A.3. ■

Theorem A.5: Let $\mathbf{x} \in \mathbb{R}^3$ and $\mathbf{D}_a^b$ and $\mathbf{D}_a^c$ be the DCMs from the *a* coordinate frame to, respectively, the *b* coordinate frame and *c* coordinate frame. If $(\mathbf{D}_a^b - \mathbf{D}_a^c)\mathbf{x} = \mathbf{0}_{3\times1}$ holds, then $\mathbf{x}$ lies in the Euler axis in which a single rotation aligns the *b* coordinate frame to the *c* coordinate frame.

Proof: The condition can be rewritten as $\mathbf{x} = \mathbf{D}_b^a \mathbf{D}_a^c \mathbf{x}$. Thus $\mathbf{x}$ is a vector that has the same representation in the *b* and *c* coordinate frames, then $\mathbf{x}$ must lie in the Euler axis in which a single rotation rotates the *b* coordinate frame into alignment with the *c* coordinate frame. ■

APPENDIX B
UAV TRAJECTORY AND ANGULAR MOVEMENT FOR SCENARIOS 04 AND 05

The UAV trajectory is composed of several segments with a distinct, constant specif force during each one. They are described in Table III.

The IMU attitude evolves as described in eqs. 31 in terms of the Euler angles that rotate the local coordinate frame into alignment with the body coordinate frame (yaw, pitch, and roll rotation sequence).

$$\begin{aligned}
\psi &= 0.1\sin\left(2\pi\frac{t}{300}\right) + 0.05\sin\left(2\pi\frac{t}{1.7}\right) \text{ rad} \\
\theta &= 0.1\sin\left(2\pi\frac{t}{300}\right) + 0.05\sin\left(2\pi\frac{t}{1.7}\right) \text{ rad} \\
\phi &= 0.1\sin\left(2\pi\frac{t}{300}\right) + 0.05\sin\left(2\pi\frac{t}{0.85}\right) \text{ rad}
\end{aligned} \tag{31}$$

TABLE II: Simulation parameters for scenarios 04 and 05.

Sensors	
$\boldsymbol{\nabla}$	$\begin{bmatrix} 3 & 3 & 3 \end{bmatrix}^T$ mg
$\boldsymbol{\epsilon}$	$\begin{bmatrix} 1000 & 1000 & 1000 \end{bmatrix}^T$ $\circ$/h
Accelerometers covariance ($\mathbf{R}_{\boldsymbol{\nabla}}$)	$diag\begin{pmatrix} 1 & 1 & 1 \end{pmatrix}(mg)^2$
Rate-gyros covariance ($\mathbf{R}_{\boldsymbol{\epsilon}}$)	$diag\begin{pmatrix} 500 & 500 & 500 \end{pmatrix}(\circ/\text{h})^2$
$\mathbf{R}_{GPS}$	$diag\begin{pmatrix} 81 & 81 & 81 & 0.1 & 0.1 & 0.1 \end{pmatrix}$ SI units^2
$\mathbf{R}_{magnetometer}$	$diag\begin{pmatrix} (2\cdot10^{-5})^2 & (2\cdot10^{-5})^2 & (2\cdot10^{-5})^2 \end{pmatrix}$ Gauss^2
Covariance of relative position measurement	$5\cdot diag\begin{pmatrix} 81 & 81 & 81 \end{pmatrix}$ m^2
GPS and magnetometer data frequency	1 Hz
INS	
Initial position	$23^\circ 12' \ S \ \ 45^\circ 52' \ W$
Initial altitude	700 m
Initial velocity	$\begin{bmatrix} 0 & 0 & 0 \end{bmatrix}^T$ m/s
Initial alignment	TRIAD algorithm
INS solution sampling rate (t_{ins})	0.01 s
Kalman filter	
Feedback start	95 s
$\mathbf{Q}$, $t < 95$ s	$diag\begin{pmatrix} \mathbf{Q}^*_{t<95\text{ s}} & 4\cdot10^{-10} & 4\cdot10^{-10} & 4\cdot10^{-10} \end{pmatrix}$ SI Units^2
$\mathbf{Q}$, $t \geq 95$ s	$diag\begin{pmatrix} \mathbf{Q}^*_{t\geq95\text{ s}} & 4\cdot10^{-10} & 4\cdot10^{-10} & 4\cdot10^{-10} \end{pmatrix}$ SI Units^2
$\mathbf{Q}^*_{t<95\text{ s}}$	$1/50\cdot t_{ins}\cdot \left[\begin{array}{cc} \mathbf{0}_3 & \mathbf{0}_3 \\ \mathbf{D}_l^b & \mathbf{0}_3 \\ \mathbf{0}_3 & -\mathbf{D}_l^b \\ \hline \multicolumn{2}{c}{\mathbf{0}_6} \end{array}\right] \cdot \begin{bmatrix} \mathbf{R}_{\boldsymbol{\nabla}} & \mathbf{0}_3 \\ \mathbf{0}_3 & \mathbf{R}_{\boldsymbol{\epsilon}} \end{bmatrix} \cdot \left[\begin{array}{cc} \mathbf{0}_3 & \mathbf{0}_3 \\ \mathbf{D}_l^b & \mathbf{0}_3 \\ \mathbf{0}_3 & -\mathbf{D}_l^b \\ \hline \multicolumn{2}{c}{\mathbf{0}_6} \end{array}\right]^T$ SI Units^2
$\mathbf{Q}^*_{t\geq95\text{ s}}$	$1/150\cdot t_{ins}\cdot \left[\begin{array}{cc} \mathbf{0}_3 & \mathbf{0}_3 \\ \mathbf{D}_l^b & \mathbf{0}_3 \\ \mathbf{0}_3 & -\mathbf{D}_l^b \\ \hline \multicolumn{2}{c}{\mathbf{0}_6} \end{array}\right] \cdot \begin{bmatrix} \mathbf{R}_{\boldsymbol{\nabla}} & \mathbf{0}_3 \\ \mathbf{0}_3 & \mathbf{R}_{\boldsymbol{\epsilon}} \end{bmatrix} \cdot \left[\begin{array}{cc} \mathbf{0}_3 & \mathbf{0}_3 \\ \mathbf{D}_l^b & \mathbf{0}_3 \\ \mathbf{0}_3 & -\mathbf{D}_l^b \\ \hline \multicolumn{2}{c}{\mathbf{0}_6} \end{array}\right]^T$ SI Units^2
Initial covariance	$diag\begin{pmatrix} 50^2 & 50^2 & 50^2 & 2^2 & 2^2 & 2^2 & 0.05 & 0.05 & 0.05 & 0.09 & 0.09 & 0.09 & 0.015 & 0.015 & 0.015 & 1 & 1 & 1 \end{pmatrix}$ SI Units^2
Initial estimate	$\mathbf{0}_{18\times1}$ SI units

TABLE III: UAVs trajectory

		Specific forces		
Start (s)	**End** (s)	**N** (m/s^2)	**E** (m/s^2)	**D** (m/s^2)
0	30	0	0	-g
30	70	+3	0	-g
70	110	0	+3	-g
110	150	+3	+3	-g
150	190	0	0	-g-3
190	240	0	0	-g
240	280	-3	0	-g
280	320	0	-3	-g
320	360	0	+2	-g
360	500	0	0	-g
500	520	0	+2	-g
520	540	-2	0	-g
540	560	-2	-2	-g
560	600	0	-2	-g
600	660	0	0	-g
660	720	0	2	-g
720	800	-2	0	-g

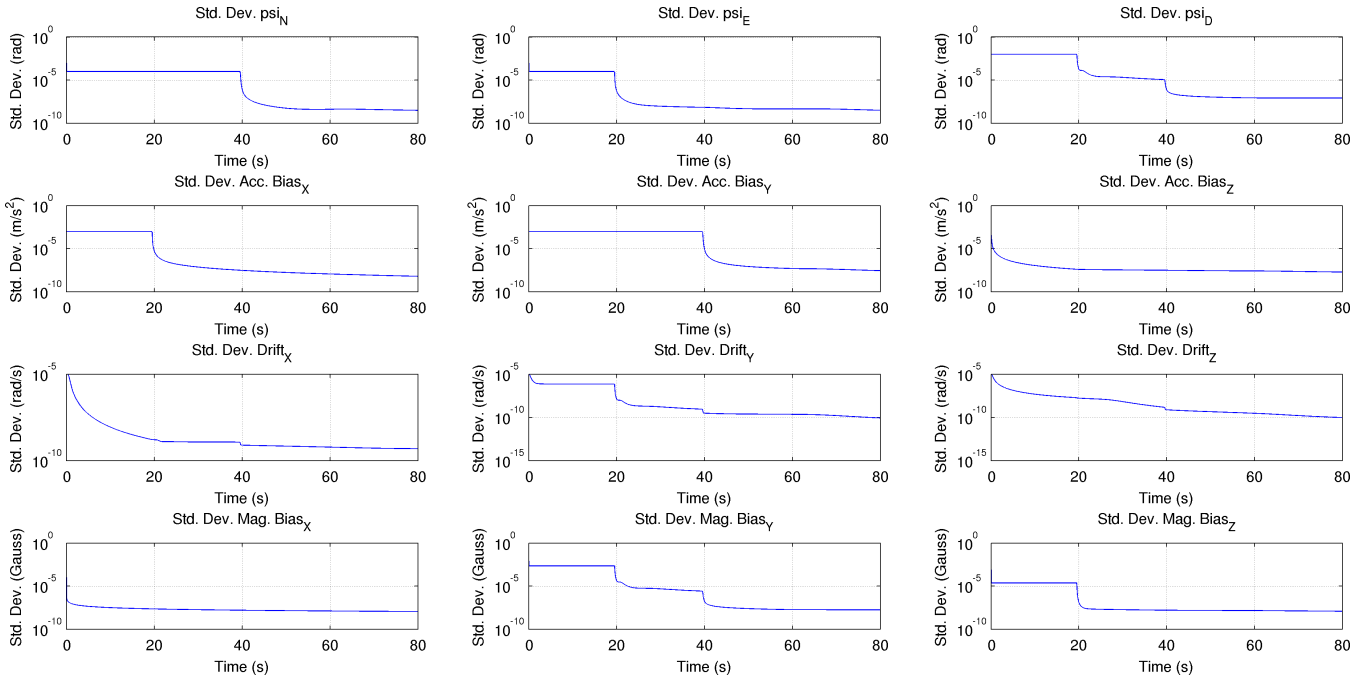

Fig. 3: Scenario 02 - Standard deviations for observability analysis with a strapdown IMU subjected to piece-wise rotations about Y-Z-X axes.

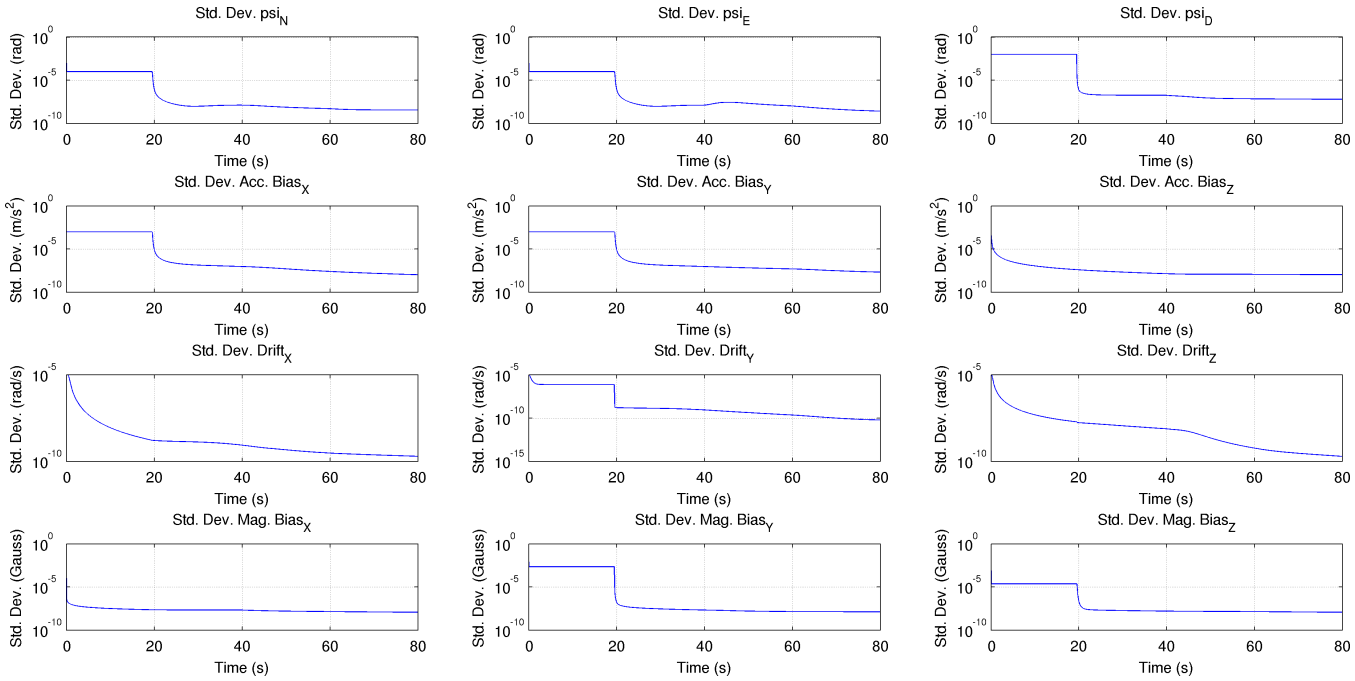

Fig. 4: Scenario 03: Standard deviations for observability analysis with a strapdown IMU subjected to piece-wise rotations about Z-Y-X axes.

One should notice that this trajectory and angular movement yield in a fully observable system according to the theoretical results in this paper.

REFERENCES

[1] I. Y. Bar-Itzhack and N. Berman, "Control theoretic approach to inertial navigation systems," *Journal of Guidance, Control, and Dynamics*, vol. 11, pp. 237–247, 1988.

[2] K. Brammer and G. Siffling, *Kalman-Bucy Filters*. United States of America: Artech House Publishers, 1989.

[3] *MTi-G User Manual and Technical Documentationz*, Xsens Technologies B.V., Pantheon 6a, P.O. Box 559, 7500 AN Enschede, The Netherlands, July 2008.

[4] *ADIS16400/ADIS16405: Triaxial Inertial Sensor with Magnetometer*, Analog Devices, Inc., One Technology Way, P.O. Box 9106, Norwood, MA 02062-9106, U.S.A., 2009.

[5] R. A. J. Chagas and J. Waldmann, "Geometric inference-

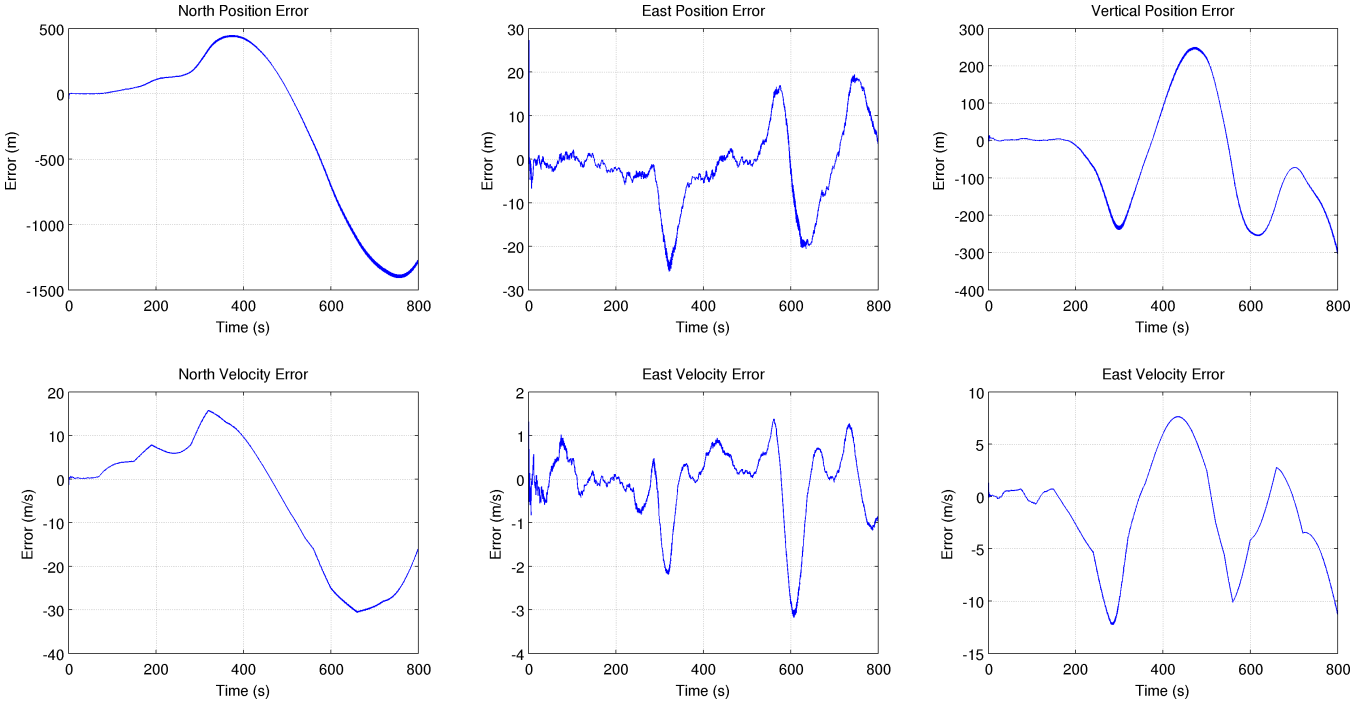

Fig. 5: Scenario 04: Estimation errors of the position and velocity errors components when the magnetometer bias is neglected.

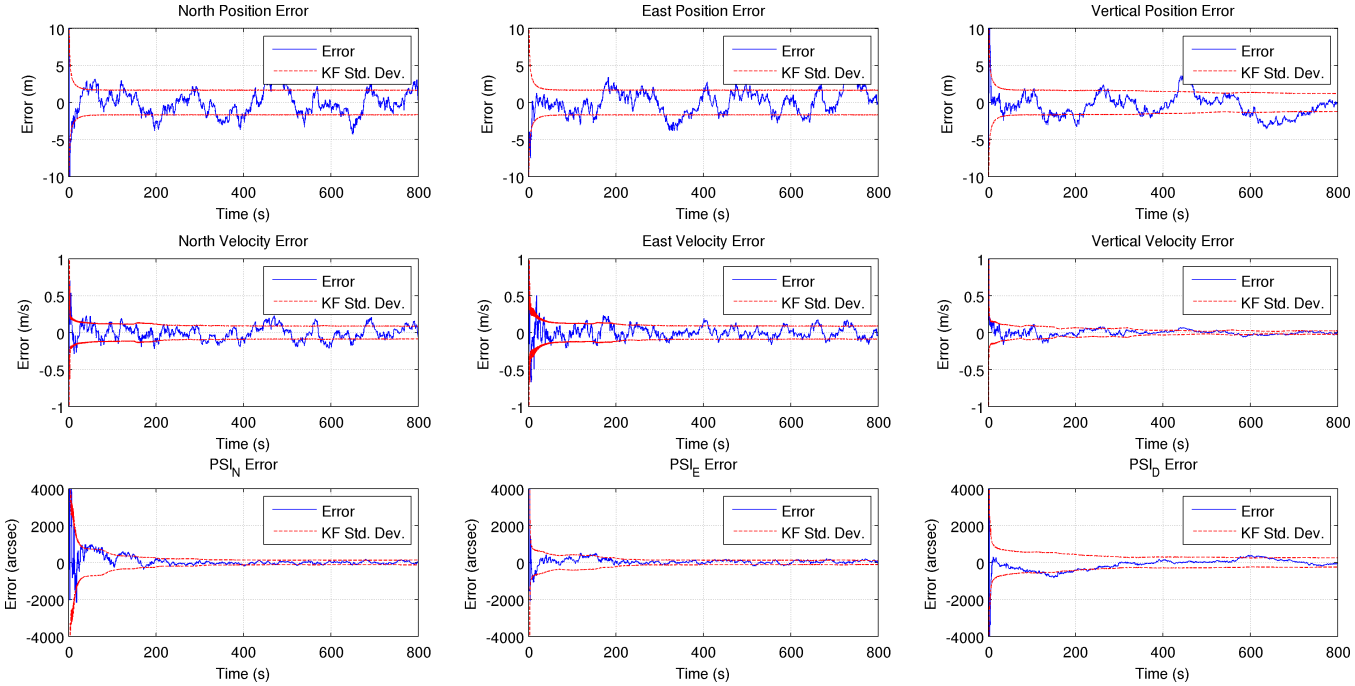

Fig. 6: Scenario 05: Estimation errors of the position, velocity, and misalignment components when the magnetometer bias is considered.

based observability analysis digest of INS error model with GPS/magnetometer/camera aiding," in *19th Saint Petersburg International Conference on Integrated Navigation Systems*, Saint Petersburg, Russia, 2012.

[6] D. Goshen-Meskin and I. Y. Bar-Itzhack, "Observability analysis of piece-wise constant systems. ii. application to inertial navigation in-flight alignment [military applications]," *IEEE Transactions on Aerospace and Electronic Systems*, vol. 28, no. 4, pp. 1068–1075, oct 1992.

[7] J. Lee, C. G. Park, and H. W. Park, "Multiposition alignment of strapdown inertial navigation system," *IEEE Transactions on Aerospace and Electronic Systems*, vol. 29, no. 4, pp. 1323–1328, 1993.

[8] O. Salychev, *Applied Inertial Navigation:Problems and Solutions*. Moscow, Russia: BMSTU Press, 2004.

[9] D. Goshen-Meskin and I. Y. Bar-Itzhack, "Observability analysis of piece-wise constant systems. i. theory," *IEEE Transactions on*

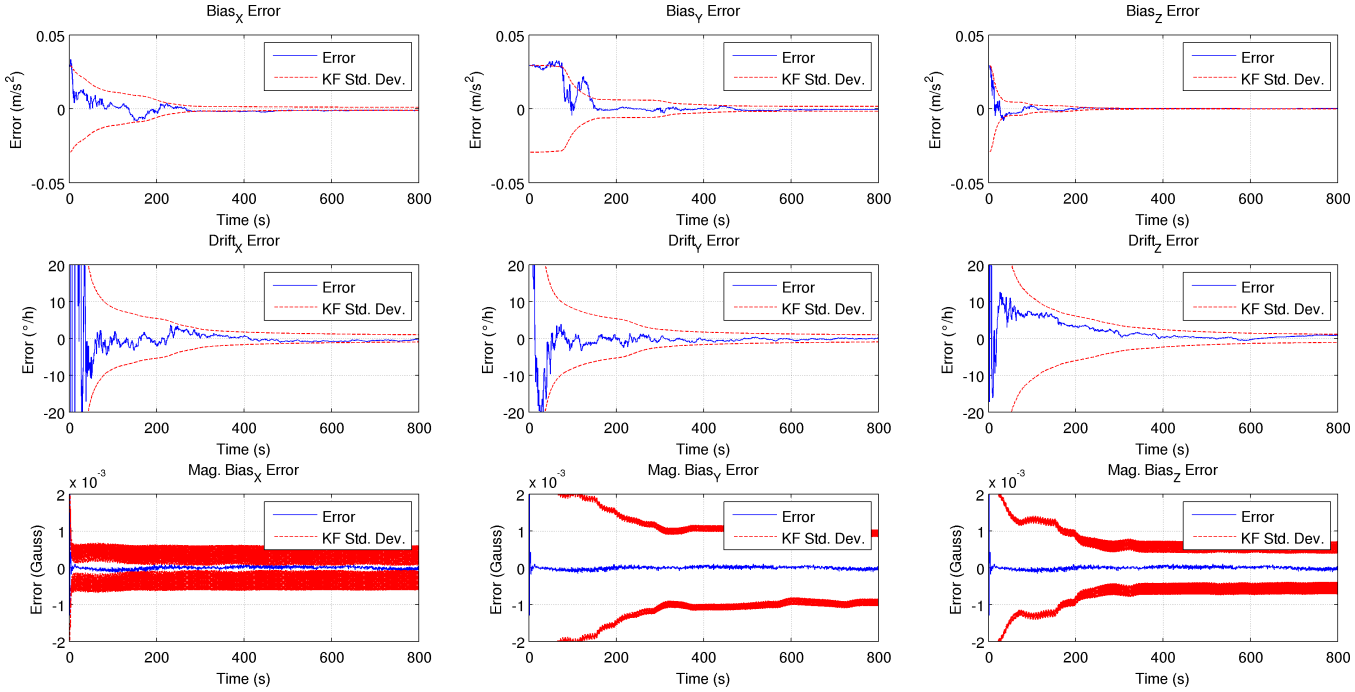

Fig. 7: Scenario 05: Estimation errors of the accelerometer bias, rate-gyro drift, and magnetometer bias components.

Aerospace and Electronic Systems, vol. 28, no. 4, pp. 1056–1067, oct 1992.

[10] J. C. Pinson, "Inertial guidance for cruise vehicles," in *Guidance and Control of Aerospace Vehicles*, C. T. Leondes, Ed. New York, United States of America: McGraw-Hill, 1963.

[11] C.-T. Chen, *Linear system theory and design*. New York, NY, United States of America: CBS College Publishing, 1984.

[12] D. Chung, C. G. Park, and J. G. Lee, "Observability analysis of strapdown inertial navigation system using Lyapunov transformation," in *35th IEEE Conference on Decision and Control*, Kobe, Japan, 1995, pp. 23–28.

[13] I. Rhee, M. F. Abdel-Hafez, and J. L. Speyer, "Observability of an integrated GPS/INS during maneuvers," *IEEE Transactions on Aerospace and Electronic Systems*, vol. 40, no. 2, pp. 526–535, 2004.

[14] S. Hong, H. C. M. H. Lee, S. Kwon, and J. L. Speyer, "Observability of erros states in GPS/INS integration," *IEEE Transactions on Vehicular Technology*, vol. 54, no. 2, pp. 731–743, 2005.

[15] M. K. Lee, S. Hong, M. H. Lee, S. Kwon, and H. Chun, "Observability analysis of alignment erros in GPS/INS," *Journal of Mechanical Science and Technology*, vol. 19, no. 6, pp. 1253–1267, 2005.

[16] Y. Tang, Y. Wu, M. Wu, W. Wu, X. Hu, and L. Shen, "Ins/gps integration: Global observability analysis," *IEEE Transactions on Vehicular Technology*, vol. 58, no. 3, pp. 1129–1142, March 2009.